https://doi.org/10.5194/egusphere-2026-4364
Preprint. Discussion started: 29 September 2026

Road Construction-Triggered Landslides: daily-resolution attribution and pre-construction suitability mapping in the Lali and Baku Gad watersheds of Himalaya, Far-Western Nepal

Bhuwan Awasthi[1*], Sarawut Ninsawat[1], Nitin Kumar Tripathi[1], Kuo-Chieh Chao[1]

[1]*Asian Institute of Technology, Thailand*

[*]*Corresponding author: st125724@ait.ac.th*

Abstract

Monsoon mountain landslide inventories face a trigger-attribution problem: failures caused by road construction can be credited to rainfall when the inventory is observed only quarterly or annually. In two adjacent watersheds in Darchula district, Far-Western Nepal where bulldozer roads began in 2017, we combined daily PlanetScope imagery (2017–2025), gauge and CHIRPS rainfall at each failure, daily road-construction records, and a quarterly inventory. Failures absent on the last clear image before a construction date and present on it were classed construction-coincident failure (CCF, n = 173 along about 69 km of road); failures mapped from 2016 imagery, before any road existed, gave a pre-road natural baseline (PRN, n = 127). Attribution proceeded by exclusion. The failures were not rainfall-driven: 63.6 % fell on dry days by gauge and 78.6 % by CHIRPS, with no rainfall correlation at any timescale. They tracked the construction front rather than the older road, 87.3 % lying within 50 m of the same-day front against 28.9 % of the old road, and they formed a distinct population, smaller and less elongate than the natural failures. One third never reached the inventory, and 60 % of those that did had failed on dry days, events a quarterly record would assign to the monsoon. Persistence was then modelled as a second-stage outcome: south-facing aspect and failure size were its dominant and most stable controls across penalised regression, Random Forest, and SHAP, and a four-variable pre-construction map placed about 90 % of persistent failures in terrain flagged unsuitable beforehand, holding on an independent watershed. Thus, daily imagery isolates a construction trigger that seasonal inventories conflate with rain, and yields a transferable basis for siting spoil before a road is cut.

Keywords: Road construction; landslide trigger attribution; PlanetScope; CHIRPS; landslide persistence; Nepal Himalaya

https://doi.org/10.5194/egusphere-2026-4364
Preprint. Discussion started: 29 September 2026

1 Introduction

In the mountains of the developing world, rural road building has become a major driver of hillslope instability, and one of the least regulated. The global road network is projected to grow by 60 % between 2010 and 2050, with the largest expansion in the high-relief terrain of South and Southeast Asia, Latin America, and sub-Saharan Africa (Laurance et al., 2014). Nepal exemplifies this trajectory. Its Local Road Network grew from 4,780 km in 1998 to 57,632 km by 2016, and road density tripled from 13.7 to 49.6 km per 100 km^2 (Sudmeier-Rieux et al., 2019). Most of this growth came from bulldozer construction without engineering oversight, drainage design, or slope stabilisation, the so-called dozer-road approach. The Nepal Rural Road Standards set no slope-excavation guidelines, and spoil disposal is unregulated (Paudyal et al., 2023; Robson et al., 2025).

The spatial link between roads and landsliding is well documented, though its strength depends on how the road is built. Near poorly constructed roads in Sindhupalchok, Nepal, rainfall-triggered landslides occur at more than twice the rate of equivalent road-free terrain (McAdoo et al., 2018), and in southern Ecuador susceptibility near highways runs an order of magnitude higher than on unroaded slopes (Brenning et al., 2015). Intensity matters too: a 23.5 km road in Yunnan, China, shed material at 9,610 t ha^{-1} yr^{-1}, far above background on adjacent slopes (Sidle et al., 2011), while more than one landslide per kilometre followed the 2022 rains along the Rishikesh–Joshimath highway in Uttarakhand, India (Mey et al., 2024). The mechanism is straightforward. Excavation strips lateral support from the uphill face and leaves oversteepened cuts, while the spoil is dumped on slopes below without compaction or drainage. Pradhan et al. (2022) showed with coupled hydro-mechanical analysis that road cuts reduce the initial factor of safety by more than 30 %, and that under the triggering rainfall the undisturbed slope retained roughly 170 % more than the cut.

Despite this evidence, the trigger of road-adjacent failures has rarely been resolved at the daily resolution that separates construction from rainfall. Existing multi-temporal inventories assign a trigger from the dominant forcing within the observation window, which is usually annual or seasonal. In a monsoon climate, where the construction season and the rainfall season coincide, this produces structural misattribution: a failure that

https://doi.org/10.5194/egusphere-2026-4364
Preprint. Discussion started: 29 September 2026

appeared on the same day as bulldozer construction, on a day with zero rainfall, is indistinguishable in any quarterly or annual record from a rainfall-triggered failure. The global fatal-landslide database of Froude and Petley (2018) records that 43 % of Nepal's fatal construction-triggered landslides occurred on road corridors, yet for non-fatal events the temporal relationship between construction and failure remains unresolved at daily resolution. Muñoz-Torrero Manchado et al. (2021) mapped 26,350 landslide events elsewhere in Far-West Nepal, of which 8,778 date to 1992–2018, and found a strong correlation between annual shallow-landslide frequency and monsoon precipitation ($r = 0.74$); annual dating, however, could not separate rainfall- from construction-triggered events.

The problem persists even where finer data exist. Harvey et al. (2025) reviewed every Nepal inventory published between 2010 and 2021 and found that construction-induced triggering is not recognised as a distinct trigger category in any of them. The NASA Landslide Hazard Assessment for Situational Awareness model likewise does not explicitly incorporate anthropogenic disturbance (Stanley et al., 2021). Even daily satellite imagery has not fully closed the gap. Emmer et al. (2022) came closest, matching daily PlanetScope imagery and daily rainfall to 56 road-corridor failures in a Peruvian catchment and finding 75 % simultaneous with construction; because freshly dumped spoil is morphologically identical to a failure scar, they could not separate genuine failures from downslope deposition of excavated material.

A second challenge concerns what happens to construction-coincident failures after the initial event. Chen et al. (2024) found that 86 % of total landslide area across the Himalaya is persistent or recurrent over a 30-year window, with an average persistence of 4.7 years and only 14 % of failures being first-time occurrences. Whether construction-coincident failures share this persistence, and what site properties control the shift from transient to persistent instability, has not been examined. The distinction matters on two counts. Scientifically, ephemeral failures that revegetate before the next quarterly mapping contribute nothing to any inventory, yet they represent real disturbance, and excluding them inflates the apparent predictive power of rainfall. Operationally, persistent failures are the subset that justifies engineering intervention such as slope retention, drainage

https://doi.org/10.5194/egusphere-2026-4364
Preprint. Discussion started: 29 September 2026

works, or route realignment; these are far cheaper to design in than to retrofit once a failure has settled into a recurring instability. The cheapest, and the one most often left to chance, is where spoil is placed, and identifying persistence-prone terrain before the cut lets that spoil be steered away from the slopes most likely to fail. No empirical, data-driven framework for pre-construction suitability assessment of road-corridor spoil disposal currently exists for the Himalayan context (Paudyal et al., 2023; Sudmeier-Rieux et al., 2019).

This study addresses both challenges in the Lali Gad and Baku Gad watersheds of Darchula District, Far-West Nepal. The objectives are: (i) to build a daily-resolution record of construction-coincident slope failures matched to rainfall and terrain attributes; (ii) to attribute or exclude rainfall as the trigger using gauge and CHIRPS records; (iii) to quantify the spatial coincidence between construction and failure; (iv) to compare construction-coincident failures against the pre-road natural baseline; (v) to demonstrate inventory-based misattribution against the quarterly inventory; (vi) to identify the predictors that separate persistent from ephemeral failures, using penalised regression with convergent validation; and (vii) to translate those predictors into a pre-construction suitability classification, validated on an independent watershed.

2 Study area

The study area is two adjacent watersheds, Lali Gad (22.1 km²) and Baku Gad (23.6 km²), covering 45.7 km² together in Darchula District, Sudurpashchim Province, Far-Western Nepal as shown in Figure 1. Relief is steep: elevations run from 467 to 2,800 m a.s.l. over short horizontal distances. Both watersheds were uniquely road-free until 2016 as shown in Figure 2; systematic bulldozer construction began in 2017 and had advanced roughly 69 km of new track by 2025, which makes the area a near-controlled setting for isolating the effect of road building on slope stability.

Geologically, the catchments lie in the Lesser Himalayan fold-thrust belt (DeCelles et al., 2001) and are underlain by four formations: the Ranimatta Formation (chloritic and sericitic phyllite), the Galyang Formation (phyllite and black slate), the Syangja Formation (dolomitic phyllite, quartzite, and slate), and the Lakharpata Formation (limestone and dolostone) (Robinson and DeCelles, 2014). Phyllite dominates the first three, and that

https://doi.org/10.5194/egusphere-2026-4364
Preprint. Discussion started: 29 September 2026

matters for what follows: when a cut face is driven through weathered phyllite, the spoil breaks down into a cohesionless muck that sits at a low angle of repose and fails readily once disturbed or wetted (Fookes et al., 1985; Hearn and Shakya, 2017).

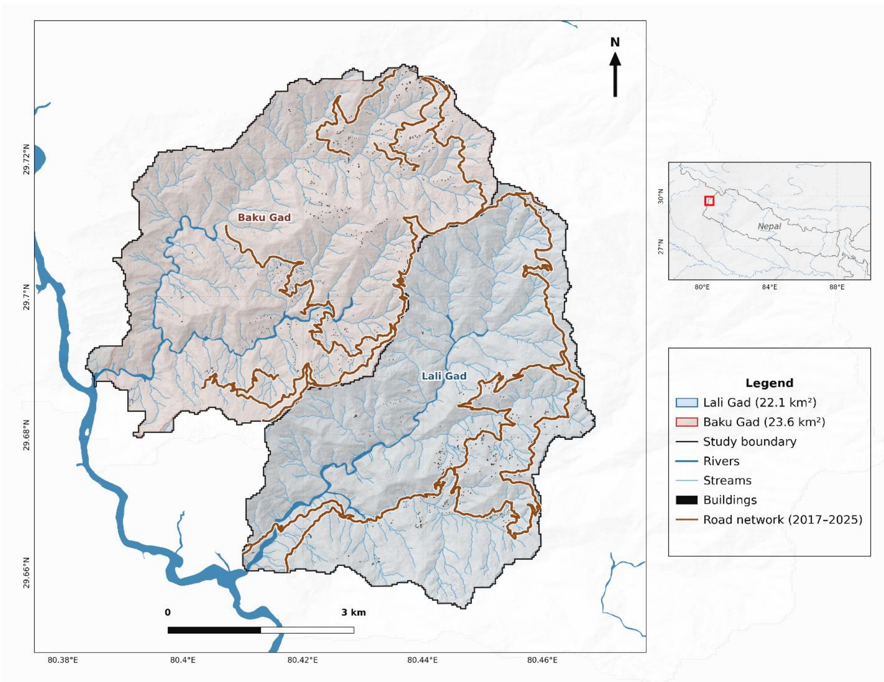

Figure 1: Study area of Lali and Baku watersheds, Far-Western Nepal

https://doi.org/10.5194/egusphere-2026-4364
Preprint. Discussion started: 29 September 2026

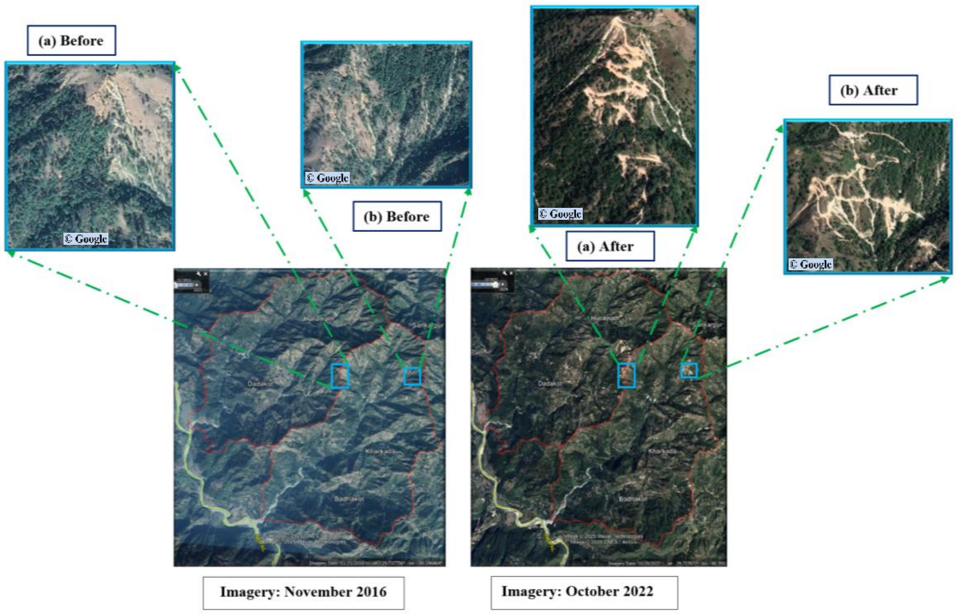

Figure 2: Google Earth imagery dated November 2016 when roads were not constructed in the terrain (left) and imagery dated October 2022 when construction were peaking (© Google).

3 Materials and methods

The methodology combines daily-resolution satellite observation with statistical attribution and persistence modelling within a geospatial analysis environment. It draws on failure mapping from daily PlanetScope imagery, two independent rainfall records, terrain attributes derived from a stereo-photogrammetric surface model, a spectral disturbance index, daily road-construction records, and a cumulative quarterly inventory. The section sets out the conceptual framework and the data, then the two analytical phases: Phase I attributes the trigger, and Phase II models persistence and maps suitability. All processing was carried out in PyGILE-Plus (Awasthi et al., 2026).

3.1 Conceptual framework

In a monsoon mountain setting the construction season and the rainfall season overlap, so the timing of a slope failure cannot, on its own, identify its cause. The same scar, on the

https://doi.org/10.5194/egusphere-2026-4364
Preprint. Discussion started: 29 September 2026

same slope, in the same months, can arise from two different processes: (i) rainfall acting on naturally unstable ground, or (ii) disturbance from road excavation and the spoil it sheds downslope. Because these processes are confounded in time, this study does not infer cause from coincidence. It assigns cause by exclusion and comparison. Rainfall is ruled out first, using gauge and satellite records on the failure date and across the antecedent windows that precede it. Construction is accepted as the most plausible trigger only where a failure satisfies three conditions together: (i) it carries no rainfall signal, (ii) it lies on the section under construction that day rather than on the older road, and (iii) it differs in form from the failures the same terrain produced before any road was cut.

This logic rests on two reference populations. The construction-coincident failure (CCF) is the unit of analysis: a failure absent from the imagery before a construction date and present on it. The pre-road natural failure (PRN), mapped from imagery taken before any road existed, is the counterfactual, that is, what a failure on this terrain looks like in the absence of construction. If CCF were simply rainfall failures that happened to fall within the construction years, they should resemble the PRN population and track rainfall. Showing that they do neither is what separates a construction trigger from a natural one.

A failure that has occurred is not yet a lasting one. Some scars revegetate before the next quarterly mapping records them, while others persist or recur over several years. The framework therefore treats persistence as a second-stage outcome that follows the trigger question: once a failure exists, whether it settles into a recurring instability is governed by the properties of the site rather than by what first disturbed it. This distinction carries the analysis from cause to consequence, and it matters on three counts: (i) persistent failures are the subset that justifies engineering intervention, so they are the ones worth anticipating; (ii) ephemeral failures never reach a quarterly inventory, yet they are real disturbance, and omitting them distorts any inventory-based account of where slopes fail; and (iii) because the trigger acts within a day while inventories record at quarterly intervals, dry-day construction failures that persist into the rainy season can be misread as monsoon failures.

https://doi.org/10.5194/egusphere-2026-4364
Preprint. Discussion started: 29 September 2026

Two hypotheses emerge. The first is that a share of the failures occurring during construction are triggered by the excavation itself rather than by rainfall, and can be isolated where rain is absent, the failure sits on the active cut, and its form departs from the natural baseline. The second hypothesis is that the persistence of these failures is governed by site conditions that are known in advance, namely slope geometry, terrain position, and structural setting, and that these controls can be expressed as a pre-construction suitability map to guide where spoil is placed and where a route is cut. The study is organised in two phases that mirror this sequence: Phase I establishes the trigger, and Phase II models persistence and translates its controls into a map. Together they move the work from explaining failures that have already happened to identifying, before a road is built, the terrain on which similar failures are most likely to last. Figure 3 sets out this framework.

https://doi.org/10.5194/egusphere-2026-4364
Preprint. Discussion started: 29 September 2026

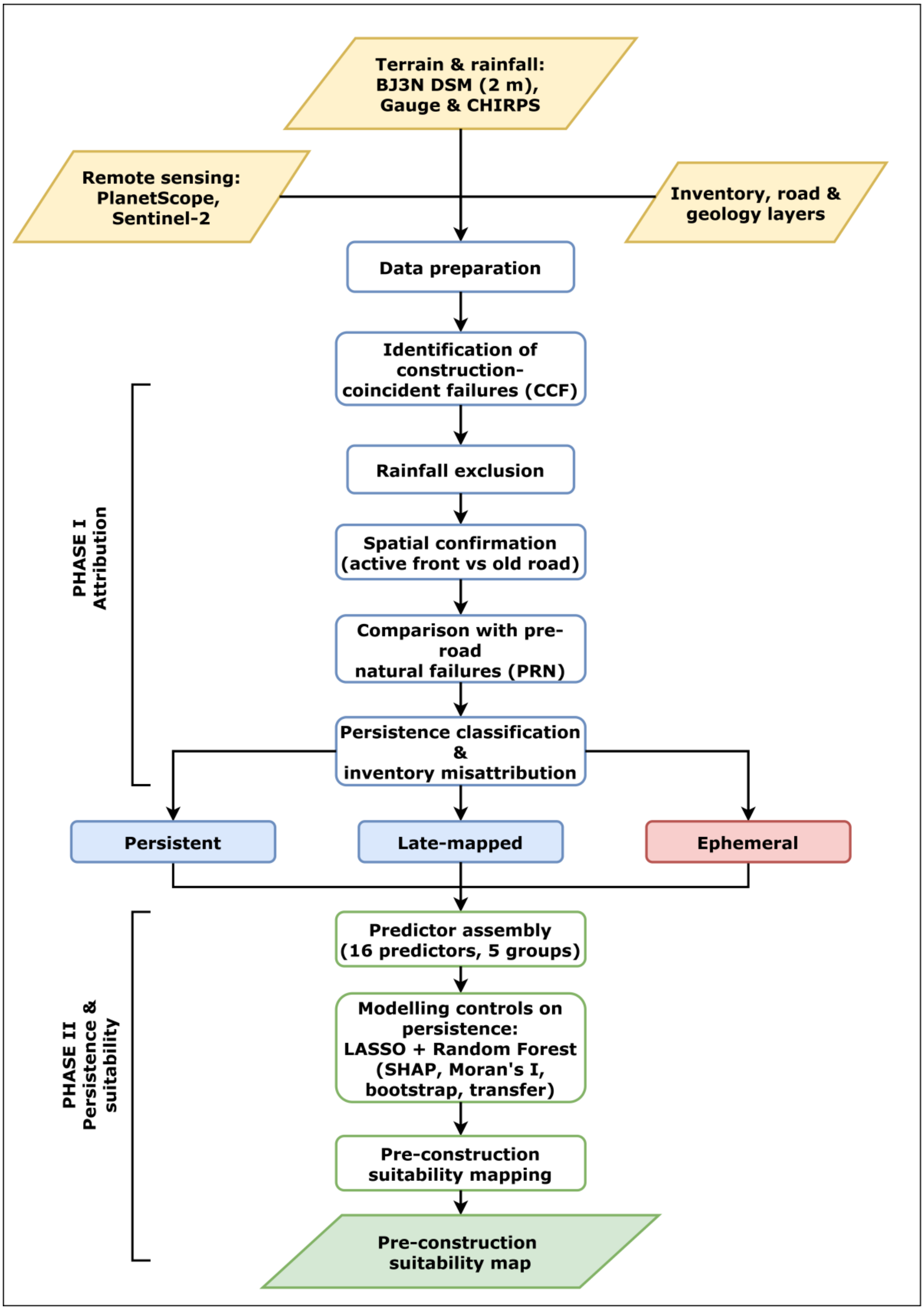

183

184 Figure 3: Methodological framework for mapping Pre-construction suitability map

https://doi.org/10.5194/egusphere-2026-4364
Preprint. Discussion started: 29 September 2026

3.2 Database

The analysis rests on seven primary datasets, summarised in

Table 1, together with supplementary geological vector data. The datasets serve four roles: (i) failure detection and dating, from PlanetScope; (ii) terrain characterisation, from the surface model; (iii) rainfall attribution, from the gauge series and CHIRPS; and (iv) construction and persistence tracking, from the road shapefiles and the quarterly inventory. The spectral disturbance index draws on Sentinel-2.

The supplementary geological data comprise polygons of the four bedrock formations introduced in the Study area, together with the thrust and fault lines from which the distance-to-thrust and distance-to-fault predictors were derived.

The terrain surface was generated in-house from satellite stereo. Four panchromatic BJ3N stereo scenes acquired on 6 February 2026 were bundle-adjusted, map-projected, and matched by dense stereo correlation in the Ames Stereo Pipeline developed by Beyer et al. (2018), and the resulting point cloud was gridded to a 2 m surface model in UTM Zone 44 N. The Copernicus GLO-30 DEM obtained through European Space Agency (2022) seeded the disparity search and provided the reference for absolute positioning. The surface was then co-registered to Copernicus over stable ground, defined as slopes below 25° with mapped landslides and roads excluded, by the Nuth and Kääb (2011) method, which removed a horizontal offset of about 2.4 m and a vertical offset of about 4.9 m. The few remaining gaps, mostly in deep shadow on steep slopes, were filled against Copernicus by a delta-surface method, and the final surface was checked against the ALOS PRISM (Tadono et al. (2014) surface and ICESat-2 ATL08 Neuenschwander and Pitts (2019) ground heights. All terrain attributes used in the analysis were derived from this surface model.

Table 1: Data utilised in the study

Source	Date	Resolution	Purpose

https://doi.org/10.5194/egusphere-2026-4364
Preprint. Discussion started: 29 September 2026

PlanetScope multispectral imagery	2017–2025	3 m, daily	Identify and date construction-coincident failures
Surface model (in-house, BJ3N stereo)	Stereo acquired 6 Feb 2026	2 m, UTM 44 N	Derive all terrain attributes
Rain-gauge series (two DHM stations)	1981–2025	Point, daily	Rainfall record at gauge location for trigger attribution
CHIRPS v2.0 Funk et al. (2015)	2016–2025	0.05°, daily	Independent rainfall check at the failure pixel
Sentinel-2 Level-2A composites (ESA)	Failure months, 2017–2025	10 m (20 m SWIR), monthly	Spectral disturbance index (NDRLI)
Road-construction shapefiles	2017–2025	Vector, daily	Locate the same-day construction front
Quarterly landslide inventory	2016–2025	Vector, quarterly mapped from 4.77 m mosaics	Classify persistence

3.3 Phase I: Attribution of construction-triggered failures

Phase I tests whether construction, not rainfall, was the primary trigger of the failures. The case is built in five steps that narrow the explanation in turn: (i) identifying the failures that coincide with construction; (ii) excluding rainfall; (iii) confirming the spatial link to the active cut; (iv) comparing the failures against the natural pre-road baseline; and (v) testing how a quarterly inventory would have attributed the same events.

https://doi.org/10.5194/egusphere-2026-4364
Preprint. Discussion started: 29 September 2026

3.3.1 Identifying construction-coincident failures

The first step builds a daily-resolution inventory of the failures that appear on the day of construction. A construction-coincident failure (CCF) is read from the change between two consecutive daily PlanetScope images (Planet Application Program Interface: In Space for Life on Earth, 2026): the scar is absent on the last clear image before a construction date and present on the image of that date. The day before construction shows an intact slope, and the construction day shows a fresh scar with freshly placed spoil at the active cut. Figure 4 follows one event in detail, the slope before and after the road and the failure absent on 9 April 2023 then present on 12 April 2023, and Figure 5 shows the same before-and-after pattern for further events between 2017 and 2025. Inspecting consecutive daily images on construction dates yielded 195 candidate failures. Candidates overlapping the 2016 pre-road inventory by more than 10 % of their area were removed as pre-existing, leaving 173 CCF. The smallest was 108.5 m^2, so every failure lay above the detection limit of the 4.77 m quarterly mosaics, spanning roughly five pixels or more.

Each failure was dated from its same-day image and checked against the catalogue of scenes on either side of the event date. A same-day image existed for all 173 failures, and the scar was clear, at or below 30 % cloud cover, on 168 of them. The last cloud-free image before the failure fell within one day for 102 failures and within three days for 167, so the median dating uncertainty was one day. Where consecutive days were not available, as in the April 2023 event, the window was set by the nearest clear images on either side and the failure date is taken as its upper bound. The deep monsoon was the exception: the 10 July 2019 failure fell on fully clouded imagery and could not be confirmed, and a further five failures had a backward gap of four days, the widest in the dataset. For these few the date is an upper bound, and for the rest it is tightly constrained.

Each identified failure was then characterised by the attributes the later steps draw on: the morphometric pair of area and length-to-width ratio, and the terrain set of slope, elevation, topographic wetness index (TWI), profile curvature, and aspect. The topographic wetness index follows Eq. (1), with β the slope in radians:

https://doi.org/10.5194/egusphere-2026-4364
Preprint. Discussion started: 29 September 2026

$$\mathrm{TWI} = \ln\left(\frac{\mathrm{SCA}}{\tan\beta}\right) \tag{1}$$

Aspect was reduced to a circular mean so that the wrap between 0° and 360° is handled correctly, as in Eq. (2):

$$\overline{\text{aspect}} = \left[\arctan 2\left(\overline{\sin\theta}, \overline{\cos\theta}\right) \times \frac{180}{\pi}\right] \backslash bmod360^\circ \tag{2}$$

A spectral measure of bare-ground disturbance, the normalised difference road-landslide index (NDRLI) after Zhao et al. (2018), was computed from the Sentinel-2 composite of each failure's month using the SWIR and blue bands, as in Eq. (3):

$$\mathrm{NDRLI} = \frac{B_{11} - B_2}{B_{11} + B_2} \tag{3}$$

These attributes fall into three groups, each a proxy for a different control: the morphometric pair for failure size and shape, the terrain set for slope-stability conditions, and the spectral index for road-induced disturbance. The step closes with a dated inventory of 173 CCF, each carrying these attributes, which the four remaining steps of Phase I test against rainfall, construction location, and the natural baseline.

https://doi.org/10.5194/egusphere-2026-4364
Preprint. Discussion started: 29 September 2026

Figure 4: A construction coincident failure before road construction and after road construction, image source Google Earth Pro VHR (© Google) 20 October 2022 (left); 8 December 2023 (right) (top); PlanetScope (© Planet Labs PBC) (below) 9 April 2023 and 12 April 2023.

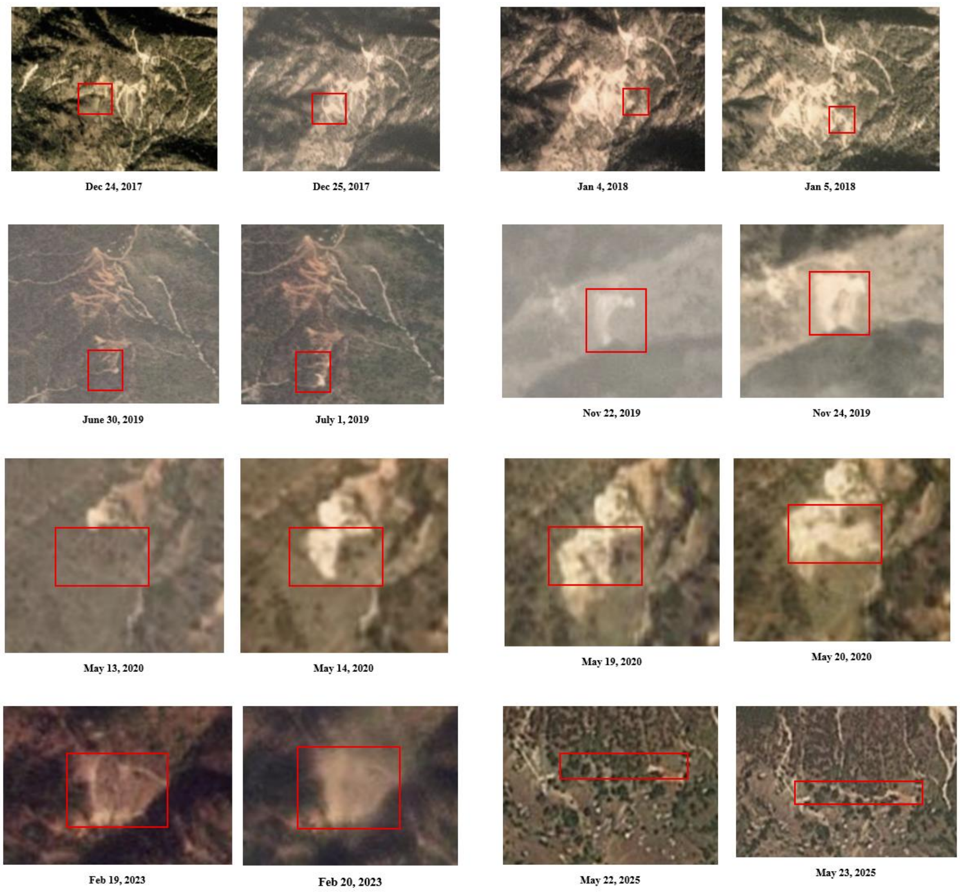

https://doi.org/10.5194/egusphere-2026-4364
Preprint. Discussion started: 29 September 2026

Figure 5: PlanetScope (© Planet Labs PBC) sample imagery showing the road construction and muck disposal on T-1, T days from 2017-2025

3.3.2 Rainfall exclusion

If rainfall had triggered these failures, they should fall on wet days or follow wet spells, so the second step tests that expectation and removes rainfall where it does not hold. Each failure was matched to the rainfall on its event date and across the 1, 3, 7, 14, and 30-day antecedent windows, under two independent records: the gauge series, and CHIRPS sampled at the failure itself. Using two records guards against either one misreading the rainfall over a given slope. Because monsoon rainfall is strongly skewed, medians and rank-based tests were used throughout: Mann-Whitney, Kruskal-Wallis, and Spearman (Guzzetti et al., 2008; Marc and Hovius, 2015). Each failure was placed in one of four event-day rainfall classes: dry at 0 mm, trace below 1 mm, low from 1 to 20 mm, and heavy above 20 mm. The rainfall and failure relationship was then examined at two resolutions, daily across all 249 road-active dates and monthly across the 56 active months, under both records.

The step yields, for every failure, an event-day rainfall class and an antecedent rainfall profile under both records, together with the daily and monthly association tests. A failure that carries no rainfall on its date and little antecedent rainfall, in records that show no association between rainfall and failure, cannot be explained by rain, which moves the explanation to the construction front tested in the next step.

3.3.3 Spatial confirmation with active road construction

Rainfall absence is necessary but not sufficient. For a failure to be attributed to construction, it must also sit on the section being cut that day rather than on the older road, so the third step tests that spatial link. For each failure, the distance from its centroid to the same-day construction front was compared with its distance to the older road network, using a Wilcoxon signed-rank test; if construction drove the failures, the same-day front should be the nearer of the two. The daily failure count was then correlated with the daily

https://doi.org/10.5194/egusphere-2026-4364
Preprint. Discussion started: 29 September 2026

length of new road, since a real construction effect should produce more failures on the days of more cutting.

One trivial explanation was ruled out before drawing that conclusion. If crews worked only on dry days, the dry-day pattern from the previous step would follow automatically, with no construction trigger needed. To check this, rainfall on the failure dates was compared against rainfall on the construction dates that produced no failure. A construction trigger requires the two to be alike; a work-scheduling artefact would instead make the failure dates the drier of the two.

The step yields, for each failure, its distance to the same-day front and to the older road, the correlation between daily failure count and new-road length, and the comparison of failure-date rainfall against no-failure construction-date rainfall. Where the failures sit closer to the active front than to the old road, and rainfall on failure and no-failure dates is alike, the dry-day clustering is not a scheduling artefact, and with rainfall already excluded the active cut stands as the trigger.

3.3.4 Comparison with pre-road natural failures

Excluding rainfall and placing the failures on the active cut points to construction, but it does not yet show that these failures differ from the ones the terrain produces on its own. The fourth step makes that comparison against a natural baseline. The pre-road natural failures (PRN), digitised from the 2016 imagery before any road existed, are the geomorphic counterfactual: what a failure on this terrain looks like in the absence of construction. The 173 CCF and the 127 PRN were compared on five attributes, area, length-to-width ratio, slope, elevation, and wetness index, using Mann-Whitney tests with the rank-biserial correlation as the effect size. The spectral index was left out of this comparison, since no Sentinel-2 composite contemporaneous with the 2016 baseline exists, so it is retained for the CCF alone. If the construction-coincident failures were merely rainfall failures that happened to fall in the construction years, they should be indistinguishable from this baseline.

The step yields a per-attribute comparison of the two populations, each attribute with its significance and effect size. A construction-coincident set that departs from the natural baseline shows these are not smaller copies of the rainfall-driven landslides but a mechanically distinct population, which closes the attribution built across the previous three steps.

3.3.5 Persistence classification and inventory-based misattribution

A failure that leaves a lasting scar and one that revegetates before the next quarterly mapping are operationally different, and only the lasting ones reach an inventory. The final step of Phase I classifies which failures persist and then shows how an inventory-based analysis would attribute them. Each CCF was matched against the cumulative quarterly inventory and classed as Persistent if it was present in the first quarter after the failure, Late-mapped if it appeared only in a later quarter, or Confirmed Ephemeral if it was never recorded. The Persistent and Late-mapped failures together form the in-inventory set, the failures an inventory-based study would see. The classification was repeated across overlap thresholds from 10 % to 30 % to confirm it was not an artefact of the threshold.

The in-inventory set was then examined by event-day rainfall class and by the quarter in which each failure was first recorded, to show what a quarterly inventory without daily dating would conclude. The rainfall-class composition reveals how many of the failures an inventory would record had in fact failed on dry days, and the recording quarter reveals which dry-day failures were first mapped in a monsoon quarter and would therefore be read as monsoon failures, when the daily evidence marks them as construction-triggered.

The step yields the persistence class of every failure, which is the outcome Phase II models, and a direct demonstration that construction-triggered dry-day failures persisting into the monsoon are the ones a quarterly inventory would misattribute to rainfall. This closes Phase I: the failures are construction-triggered, and an inventory alone would have assigned them to the wrong cause.

https://doi.org/10.5194/egusphere-2026-4364
Preprint. Discussion started: 29 September 2026

3.4 Phase II: Persistence modelling and suitability mapping

Phase II asks what makes a construction-triggered failure persist rather than fade, and turns the answer into a map that can be read before a road is built. It runs in three steps: assembling the predictors, modelling which of them control persistence, and translating the stable controls into a pre-construction suitability map.

3.4.1 Predictor assembly

The model needs a set of candidate properties that might separate the persistent failures from the ephemeral ones. The candidates were drawn across five groups, each standing for a different kind of control: morphometric, the failure's size and shape (area and length-to-width ratio); topographic, the slope and its setting (slope, elevation, wetness index, profile curvature, and aspect); rainfall and timing, the conditions around the failure date; geological, the structural setting through distance to thrust and to fault; and construction, the failure's relation to the active works. These draw on sources already introduced: the morphometric and topographic predictors are the attributes attached at identification, the geological predictors from the structural lines, the rainfall and timing predictors from the two rainfall records, and the construction predictors from the daily road shapefiles.

This candidate pool was reduced before modelling to remove redundancy and incomplete coverage. Where two candidates were strongly correlated ($|r| > 0.70$), only one was carried forward, so the penalised fit would not split a single signal between near-duplicates: plan curvature, the 30-day antecedent and 30-day post-event rainfall totals, and a rainfall-timing candidate were dropped on this basis, each against a retained predictor holding the same information. The spectral disturbance index was set aside because it was not available for every failure (148 of 173). This left sixteen predictors, with the persistence class from the previous step as the response they are assembled to explain.

3.4.2 Modelling the controls on persistence

With the predictors assembled, the question is which of them separate the failures that persist into the inventory from the ephemeral ones. A LASSO logistic regression was fitted to the persistence outcome, with the penalty strength chosen by ten-fold cross-validation

https://doi.org/10.5194/egusphere-2026-4364
Preprint. Discussion started: 29 September 2026

over a grid of values and with class weighting to offset the 115 to 58 imbalance between in-inventory and ephemeral failures. The penalty does double duty: it selects the predictors that carry signal, and it guards against the low events-per-variable ratio, here 3.6, which would otherwise risk an overfitted model (Peduzzi et al., 1996; van Smeden et al., 2019).

Because a single model can mislead, three independent checks were run, each for a stated reason. A Random Forest with permutation importance tests whether the predictor ranking survives a non-linear model. SHAP values give the per-failure contribution behind that ranking. Moran's I on the residuals tests for unexplained spatial structure, which would breach the model's independence assumption. The coefficients were then refit on 1,000 bootstrap samples to measure how stable each predictor is, and finally the model was trained on one watershed and applied to the other to test whether it transfers.

The step yields the set of predictors that control persistence, ranked and with their stability, confirmed against a non-linear model and checked for residual spatial structure and for transfer between watersheds. The predictors that prove both influential and stable, and that describe the site rather than the event, are the ones carried into the suitability map.

3.4.3 Pre-construction suitability mapping

A persistence model is only useful before a road is built if it rests on what can be known in advance. The final step turns the stable controls into a map a planner can read at the design stage. Of the predictors the model retained, four describe the site rather than the event: aspect, slope, distance to thrust, and elevation. Only these were carried into the map, because a map made before construction cannot use a property of a failure that has not yet occurred, such as its size. Each of the four was scaled to a common range and combined using the model's coefficients as weights, as in Eq. (4):

$$S = 0.458 \cdot \cos_{\mathrm{aspect,norm}} + 0.211 \cdot \mathrm{slope}_{\mathrm{norm}} + 0.129 \cdot \mathrm{thrust}_{\mathrm{norm}} + 0.202 \cdot \mathrm{elev}_{\mathrm{norm}} \qquad (4)$$

Two physical limits override the score. Slopes above 35°, beyond the angle of repose for loose spoil, and ground within 50 m of a channel, where debris reaches the stream, are

https://doi.org/10.5194/egusphere-2026-4364
Preprint. Discussion started: 29 September 2026

treated as unsuitable regardless of the weighted score. Each pixel was then classed as Suitable, Marginal, or Unsuitable.

The result is a suitability surface over the whole catchment, classed into three zones. It was first assessed on the full sample of failures, then validated by deriving the weights from one watershed and scoring them against the failures of the other, which the weights had never seen, so that the test measures transfer rather than fit.

4 Results

4.1 Attribution of construction-triggered failures

The results are organised in two phases. Phase I establishes that the failures are construction-triggered; Phase II identifies what controls their persistence and renders it as a map. Three findings carry the study. First, the failures are not rainfall-driven: 63.6 % occurred on days with no recorded rain, and rainfall shows no association with failure at either daily or monthly resolution. Second, they track the active construction front rather than the existing road: 87.3 % lie within 50 m of the same-day cut, against 28.9 % within 50 m of the older network. Third, their persistence is predictable from terrain knowable before a road is built, with south-facing aspect and failure size the dominant and most stable controls, and the model holding on an unseen watershed. Sections 4.1.1 to 4.1.5 present the Phase I evidence, and 4.2.1 to 4.2.3 the Phase II model and map.

4.1.1 The construction-coincident failure inventory

Daily mapping across 2017 to 2025 yielded 173 construction-coincident failures, screened from 195 candidates after 22 that overlapped the 2016 pre-road inventory were removed as pre-existing. The pre-road baseline comprised 127 natural failures mapped before any road existed. Failures occurred in every construction year and peaked in the years of heaviest cutting, 40 in 2020 and 36 in 2019, with the annual sequence running 22, 9, 36, 40, 18, 23, 23, 1, and 1; the single failures of 2024 and 2025 reflect minimal mapped construction in those years shown in Figure 6. Most fell in the dry season, 125 of 173 (72.3 %) between October and May, against 48 of 173 (27.7 %) in the monsoon.

https://doi.org/10.5194/egusphere-2026-4364
Preprint. Discussion started: 29 September 2026

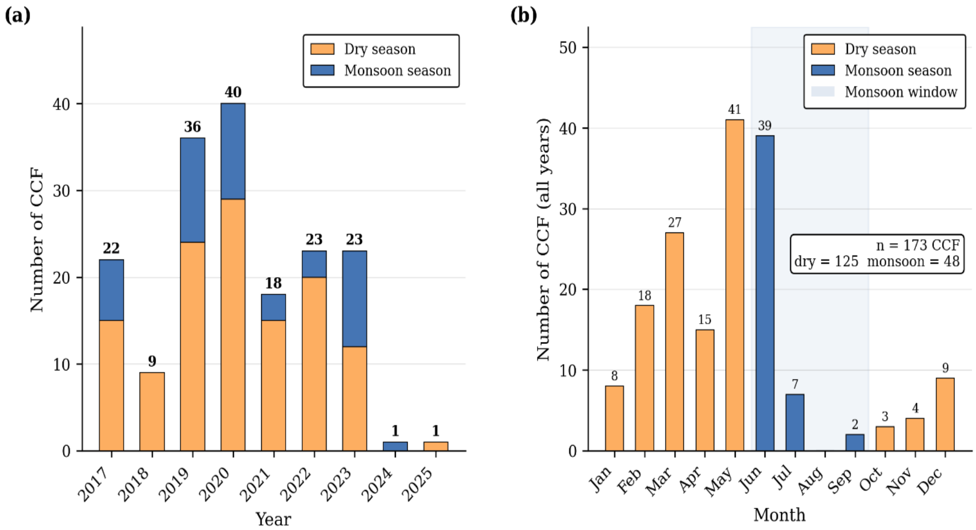

Figure 6: Temporal distribution of CCF. (a) Annual totals 2017–2025 stacked by season. (b) Monthly totals across the full period, stacked by season.

4.1.2 Failures are not rainfall-driven

The failures did not fall on rainy days. Under the gauge record, 110 of 173 (63.6 %) occurred on days with no recorded rainfall and 133 (76.9 %) on effectively dry days below 1 mm; only three fell on heavy-rain days above 20 mm, and all three were in the dry season, none in the monsoon (Figure 7; Table 2). CHIRPS, sampled at the failure pixel rather than at the lateral gauges, placed even more of them on dry days, 136 of 173 (78.6 %) at zero rainfall. Where the two records disagree they do so asymmetrically, and in the direction that strengthens the reading: the gauges more often registered rain that did not reach the failure site (41 of 173) than missed local rain at it (15 of 173), so the failure pixels were, if anything, drier than the gauge suggests.

Rainfall and failure were uncorrelated at both resolutions and under both records. At daily resolution across all 249 road-active dates, the Spearman correlation between rainfall and failure count was −0.018 under the gauge and +0.030 under CHIRPS, both non-significant against a minimum detectable correlation of 0.125 at this sample size; aggregated to the 56 active months it was +0.099 and +0.177, again non-significant. Antecedent rainfall on the 110 dry-day failures was likewise low, a median of 6.7 mm over the preceding seven days,

https://doi.org/10.5194/egusphere-2026-4364
Preprint. Discussion started: 29 September 2026

and failure size and shape did not vary with rainfall class (Kruskal-Wallis p = 0.285 and 0.204). On every test, at every timescale, and under two independent rainfall records, rainfall does not explain when the failures occurred.

Table 2: Gauge versus CHIRPS daily rainfall attribution for the CCF.

Metric	Gauge	CHIRPS
Zero-rain day (= 0 mm)	63.6 %	78.6 %
< 1 mm day	76.9 %	79.8 %
Median 7-day antecedent	6.7 mm	6.7 mm
Median 14-day antecedent	24.1 mm	11.2 mm
Median 30-day antecedent	52.6 mm	29.0 mm
Monthly Spearman ρ (n = 56)	0.099	0.177
Concordance on zero classification	-	67.6 %

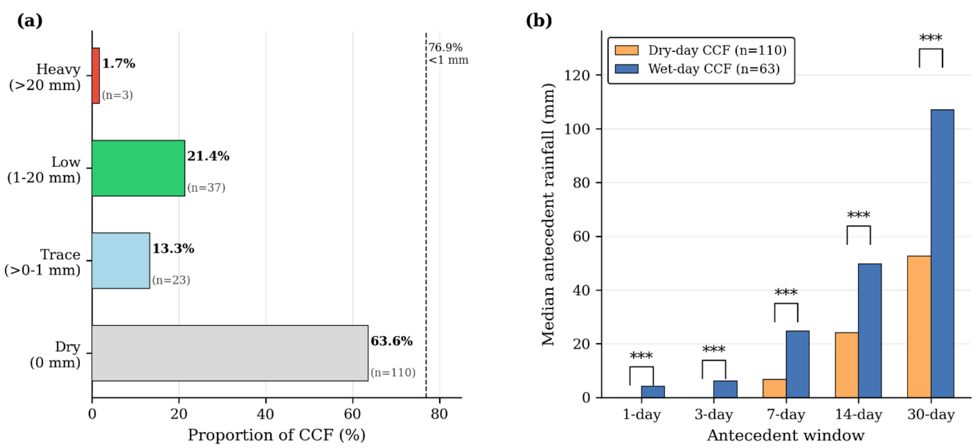

Figure 7: Rainfall attribution of CCF. (a) Distribution of CCF across the four event-day rainfall classes, separated by season (gauge). (b) Antecedent rainfall distributions for the 110 dry-day CCF, in 7-, 14-, and 30-day windows.

https://doi.org/10.5194/egusphere-2026-4364
Preprint. Discussion started: 29 September 2026

4.1.3 Failures track the construction front, not the existing road

The failures cluster on the section being cut that day, not on the older road. A failure centroid sat a median of 29.2 m from the same-day construction front but 92.5 m from the prior road network, and 151 of 173 (87.3 %) lay within 50 m of the active front against only 50 (28.9 %) within 50 m of the older road; by 100 m the gap was 170 of 173 (98.3 %) against 95 (54.9 %) shown in Figure 8. The failures were significantly closer to the active front than to the existing road (Wilcoxon signed-rank $W = 527.0$, $p < 0.001$, $n = 173$). The count of failures on a given day also rose with the length of new road cut that day, weakly across all 249 road-active dates ($\rho = +0.126$, $p = 0.046$) and more strongly on the 94 dates that produced a failure ($\rho = +0.552$, $p < 0.001$).

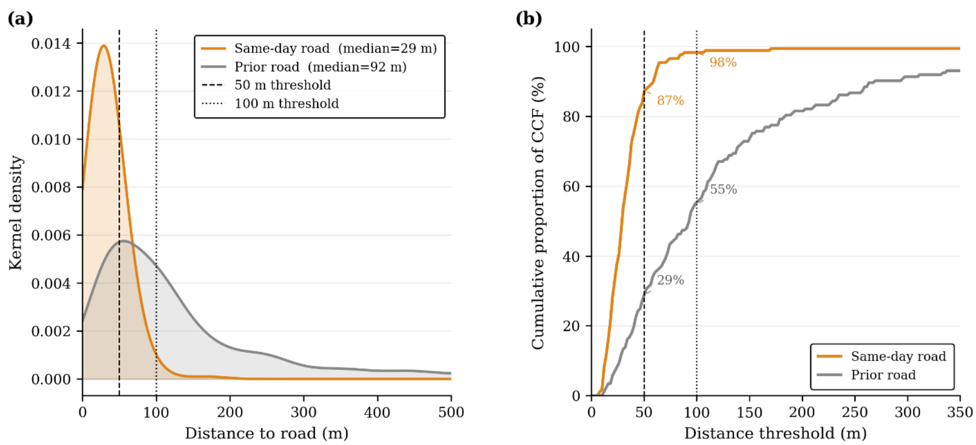

Figure 8: Spatial coincidence between CCF and road construction. (a) Kernel density of centroid distances to the same-day construction front and to the prior road network. (b) Cumulative proportion of CCF within increasing distance bands

This clustering is not an artefact of crews working only on dry days. Rainfall on the 94 failure dates was indistinguishable from rainfall on the 155 construction dates that produced no failure, a median of 0 mm in both under each record (Mann-Whitney $p = 0.52$ gauge, $p = 0.66$ CHIRPS). Construction proceeded on wet and dry days alike, so the dry-day clustering of the failures reflects the construction trigger, not a behavioural choice of which days were worked.

https://doi.org/10.5194/egusphere-2026-4364
Preprint. Discussion started: 29 September 2026

4.1.4 Construction-coincident failures are a distinct population from the natural baseline

The construction failures are not simply smaller versions of the landslides this terrain produces on its own. They differ from the pre-road natural failures on four of the five attributes tested given in (Table 3; Figure 9): far smaller in area (median 1,379 m² against 6,369 m²; r_rb = −0.764) and much less elongate (length-to-width 1.60 against 2.48; r_rb = −0.535), and on slightly gentler (37.4° against 39.1°; r_rb = −0.186) and wetter ground (TWI 3.65 against 3.47; r_rb = +0.152). All four differences are significant after correction; only elevation does not separate the two populations (1,322 m against 1,279 m; p_adj = 0.503). They are a distinct population of compact failures on convergent, topographically wetter ground, not smaller copies of the natural landslides as depicted in Figure 10.

Table 3: Morphometric and terrain comparison of CCF versus PRN. Two-sided Mann–Whitney U with BH-FDR correction.

Feature	CCF median	PRN median	p_{adj}	r_{rb}	Sig.
Area (m²)	1,379	6,369	< 0.001	−0.764	yes
L/W ratio	1.604	2.480	< 0.001	−0.535	yes
Slope (°)	37.4	39.1	0.010	−0.186	yes
Elevation (m)	1,322	1,279	0.503	+0.045	no
TWI	3.649	3.472	0.031	+0.152	yes

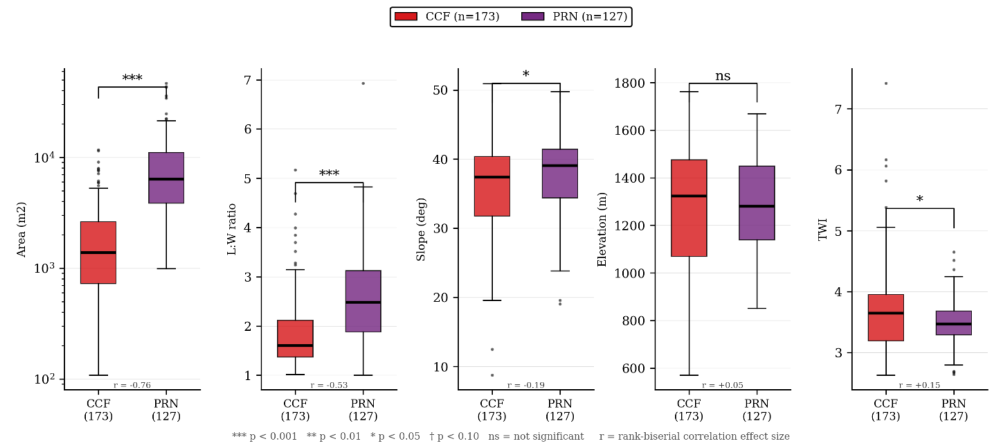

Figure 9: Boxplots comparing CCF (n = 173) and PRN (n = 127) on area, L/W ratio, slope, elevation, and TWI.

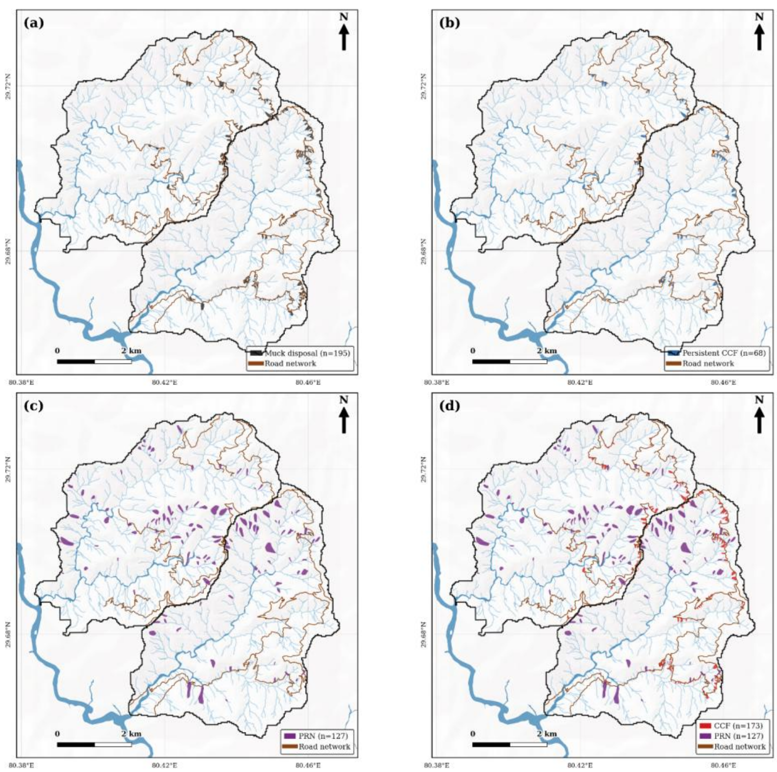

Figure 10: Spatial distribution of muck disposal (a); persistent CCF (b); pre-existing natural landslides (c); comparative CCF vs PRN (d).

https://doi.org/10.5194/egusphere-2026-4364
Preprint. Discussion started: 29 September 2026

4.1.5 Persistence and inventory-based misattribution

A third of the failures left no lasting trace. Of the 173, 68 (39.3 %) were Persistent, recorded in the first quarterly inventory after they occurred, 47 (27.2 %) were Late-mapped, appearing only in a later quarter, and 58 (33.5 %) were Confirmed Ephemeral, never recorded at all; the 115 (66.5 %) that did enter the inventory are the Persistent and Late-mapped together. This split is robust to the matching rule: the ephemeral fraction varied only between 31.8 % and 34.1 % across overlap thresholds from 10 % to 30 % depicted in Figure 11.

The failures an inventory would record are mostly dry-day failures. Of the 115 in-inventory failures, 69 (60.0 %) occurred on days with no rain and 84 (73.0 %) on days below 1 mm, so any inventory-based analysis would carry a large set of construction-triggered failures and, lacking daily dating, could read them as rainfall-driven. The clearest case is the monsoon quarter: of the five failures triggered between July and September and confirmed as Persistent, three occurred on dry construction days, yet a quarterly inventory would record them among monsoon failures. The daily evidence marks them as construction-triggered; an inventory alone would assign them to the rainfall.

4.2 Persistence modelling and suitability mapping

4.2.1 Predictor screening

Before any model was fitted, each candidate predictor was examined on its own for how well it separated persistent from ephemeral failures, as an orientation to what the model would later weigh (Figure 12). Five stood out. Persistent failures are larger (area, $r_{rb} = +0.364$; $p_{adj} = 0.002$) and on steeper ground (slope, $r_{rb} = +0.293$; $p_{adj} = 0.020$), the two clearest single separations. Three more follow at a more lenient threshold: persistent failures sit higher (elevation, $r_{rb} = +0.245$), nearer the mapped thrusts (distance to thrust, $r_{rb} = -0.240$), and on more southerly slopes (cos(aspect), $r_{rb} = -0.238$), each at $p_{adj} = 0.052$. The aspect signal is the one to carry forward: the median cos(aspect) is −0.668 for persistent failures against −0.412 for ephemeral ones, a southerly orientation, since cos(aspect) runs from +1 at due north to −1 at due south.

https://doi.org/10.5194/egusphere-2026-4364
Preprint. Discussion started: 29 September 2026

These are single-variable associations, not the model itself; they describe each predictor in isolation and do not yet account for the overlap between them. The next section fits all the predictors together and tests whether this ordering survives.

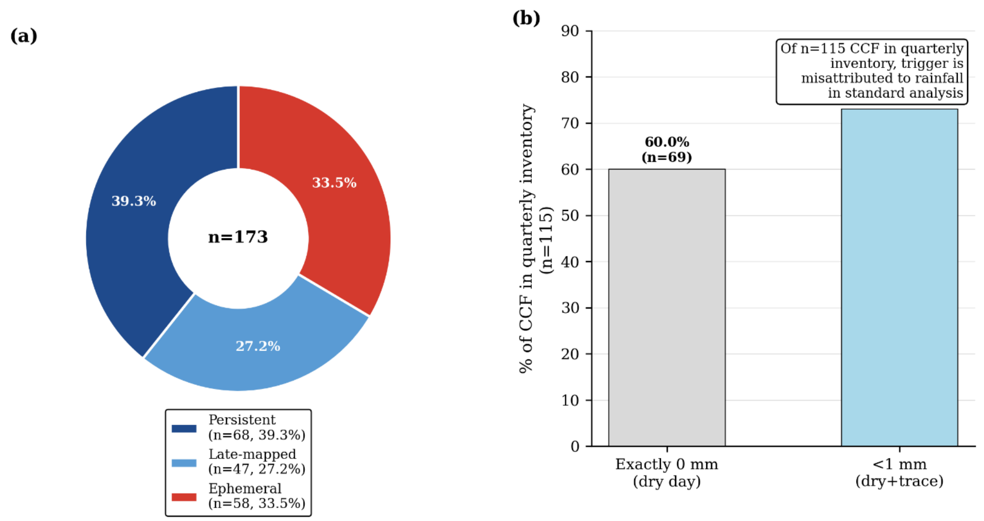

Figure 11: Persistence classification and inventory misattribution. (a) Three-category breakdown of the 173 CCF. (b) Misattribution bars: rainfall-class composition of the 115 in-inventory CCF (Persistent + Late-mapped combined).

4.2.2 Persistence is predictable, with south-facing aspect and failure size the dominant stable controls

Whether a construction failure persists or fades is predictable from a small set of controls, and two dominate: south-facing aspect and failure size. In the penalised model, cos(aspect) carried the largest coefficient ($\beta = -0.632$, the negative sign marking a southerly orientation) and area the next ($\beta = +0.530$), and these were also the most stable of all the predictors: cos(aspect) was retained in every one of 1,000 bootstrap fits (100 %) and area in 98 % (Table 4; Figure 13). The LASSO kept 14 of the 16 predictors at the cross-validated penalty ($C = 1.26$), zeroing only length-to-width ratio and 7-day antecedent rain.

The ranking holds across methods. A Random Forest with permutation importance and SHAP returned the same top two, failure size then south-facing aspect (mean SHAP contributions 0.083 and 0.054; Figure 14) so the result is not an artefact of the linear model.

https://doi.org/10.5194/egusphere-2026-4364
Preprint. Discussion started: 29 September 2026

The residuals carried no unexplained spatial structure (Moran's I = −0.011, p = 0.45), and every retained predictor was non-zero in at least 87.7 % of the bootstrap fits, so the signal is stable rather than a product of one sample.

The controls also transfer between watersheds. Trained on Lali Gad alone and applied to the unseen Baku Gad failures, the model held an AUC of 0.690 (95 % CI 0.538 to 0.804), close to its full-sample value, evidence that the same controls operate beyond the slopes they were learned on.

Discrimination itself is modest, and much the same across approaches: AUC 0.709 for the LASSO, 0.727 for the Random Forest, and 0.711 for a four-predictor model built on the mappable variables alone, against 0.666 for failure size on its own tabulated in Table 5.

These differences sit within the sampling noise of 173 cases. The value of the model is therefore not sharp prediction of individual outcomes but the identification of which controls carry stable, transferable signal, and it is the four mappable controls among them that the suitability map is built on.

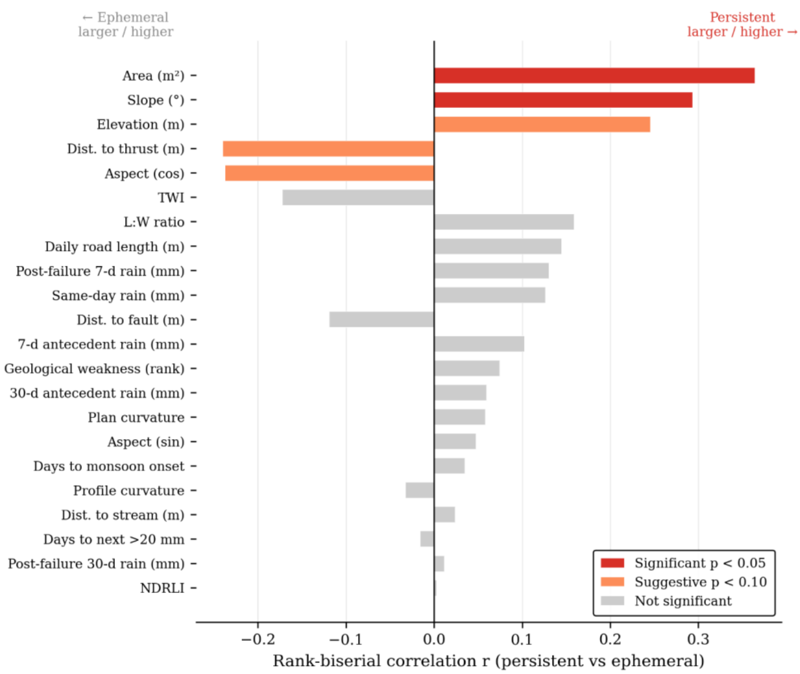

Figure 12: Univariate effect sizes

https://doi.org/10.5194/egusphere-2026-4364
Preprint. Discussion started: 29 September 2026

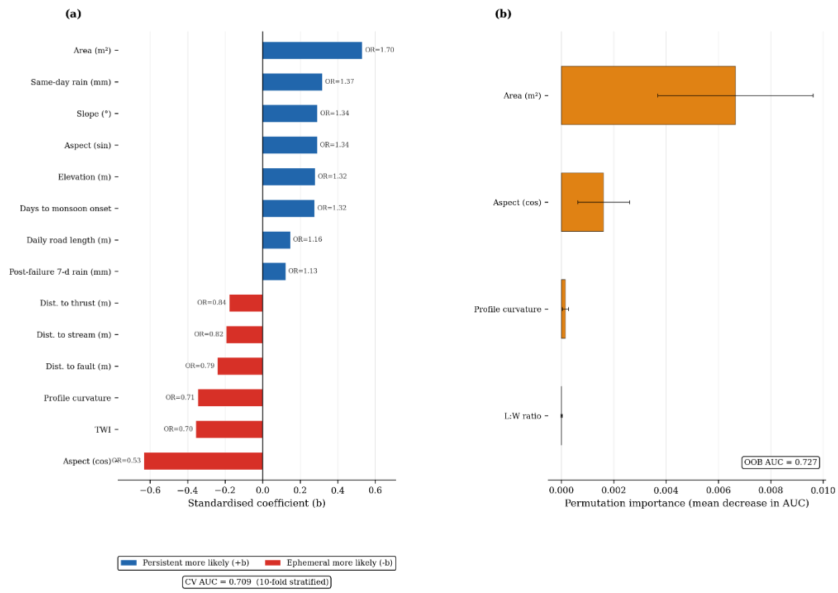

Figure 13: LASSO coefficients and RF importance

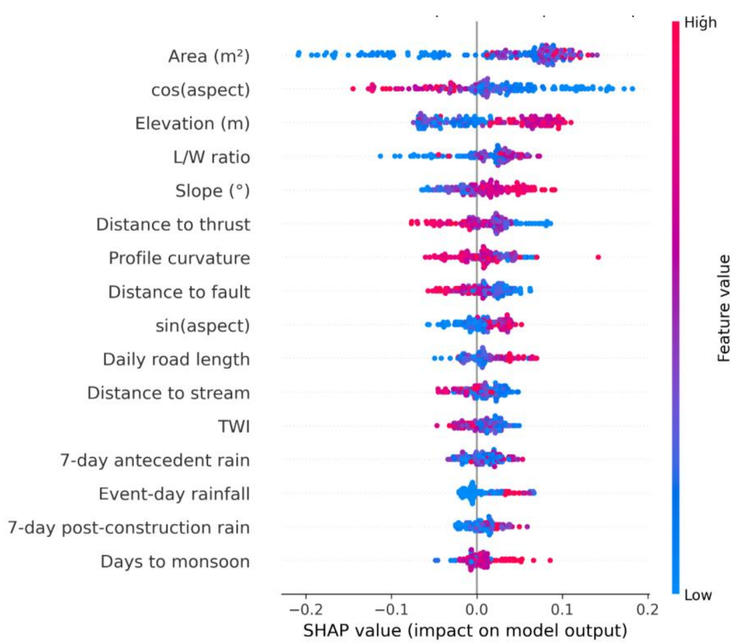

Figure 14: SHAP summary plot for the Random Forest persistence classifier.

https://doi.org/10.5194/egusphere-2026-4364
Preprint. Discussion started: 29 September 2026

Table 4: Non-zero LASSO predictors: coefficients, ORs, bootstrap intervals, selection stability

Predictor	β (std)	95 % CI β	OR (1 SD)	95 % CI OR	Stability
cos(aspect)	−0.632	[−1.194, −0.297]	0.531	[0.303, 0.743]	100.0 %
area (m²)	+0.530	[+0.000, +1.466]	1.699	[1.000, 4.330]	98.0 %
twi	−0.355	[−1.036, +0.087]	0.701	[0.355, 1.091]	95.0 %
profile curvature	−0.346	[−0.901, +0.000]	0.708	[0.406, 1.000]	96.8 %
rain day (mm)	+0.317	[−0.043, +1.022]	1.373	[0.958, 2.777]	95.4 %
Slope (deg)	+0.291	[−0.146, +0.962]	1.337	[0.865, 2.616]	91.0 %
sin(aspect)	+0.290	[−0.026, +0.845]	1.337	[0.974, 2.328]	96.2 %
Elevation (m)	+0.279	[−0.142, +0.916]	1.322	[0.867, 2.498]	93.1 %
days to monsoon	+0.275	[−0.079, +0.789]	1.317	[0.924, 2.202]	95.7 %
distance to fault (m)	−0.241	[−0.698, +0.066]	0.786	[0.498, 1.069]	95.3 %
distance to stream (m)	−0.194	[−0.715, +0.185]	0.824	[0.489, 1.203]	91.9 %

https://doi.org/10.5194/egusphere-2026-4364
Preprint. Discussion started: 29 September 2026

distance to thrust (m)	−0.178	[−0.628, +0.175]	0.837	[0.534, 1.191]	92.7 %
road length day (m)	+0.147	[−0.300, +0.867]	1.158	[0.741, 2.380]	90.4 %
post rain (7d)	+0.122	[−0.491, +0.914]	1.130	[0.612, 2.495]	87.7 %

Table 5: Model performance summary under common CV

Model	**Predictors**	**CV AUC**	**Note**
Stratified random (B0)	0	0.512	floor
Majority dummy (B1)	0	0.500	always predicts persistent
Logistic, cos(aspect) only (B4)	1	0.572	single best stability predictor
Logistic, slope only (B3)	1	0.641	single univariate predictor
Logistic, area only (B2)	1	0.666	strongest univariate predictor
LASSO 16-predictor (M)	**16**	**0.709**	**reference; 14 retained at CV-selected C = 1.26**
Logistic, 4 mappable (B5)	4	0.711	post-hoc; selected by LASSO
LASSO training AUC	16	0.797	upper bound; optimism = 0.088
Random Forest (OOB)	16	0.727	500 trees, class-balanced
LASSO LOWO (Lali → Baku)	16	0.690	validated on Baku Gad (n = 63); 95 % CI 0.538–0.804

https://doi.org/10.5194/egusphere-2026-4364
Preprint. Discussion started: 29 September 2026

Moran's I on residuals	—	−0.011	p = 0.451; 2,000 m band; 999 permutations

4.2.3 Pre-construction suitability and validation

The terrain most prone to persistent failure can be identified before a road is cut. Two physical limits remove most of the catchment before any score is applied: slopes above 35°, beyond the angle of repose for loose spoil, exclude 46.8 %, and ground within 50 m of a channel excludes 39.2 %, together ruling out 69.0 %. The weighted score as given in Eq. (4) divides the remainder into three zones: Suitable (9.9 %, 457.3 ha), Marginal (16.0 %, 737.6 ha), and Unsuitable (74.1 %, 3,425.9 ha) (

Table 6; Figure 15).

Because most of the catchment is Unsuitable, 86.1 % of all failures fall in that zone, so the test is not where failures land overall but whether the persistent and ephemeral classes separate. They do: 90.4 % of persistent failures (104 of 115) fall in Unsuitable terrain, against 77.6 % of the ephemeral ones (45 of 58).

The separation holds on ground the map was not built from. Weights derived from Lali Gad alone, applied to the unseen Baku Gad failures, placed 90.0 % of its persistent failures in Unsuitable terrain against 65.2 % of its ephemeral ones as shown in Figure 16, and separated the two classes on the continuous score (Mann-Whitney, $p = 0.002$). The four pre-construction variables therefore identify persistence-prone ground before any excavation, and they do so on a watershed the weights had never seen.

https://doi.org/10.5194/egusphere-2026-4364
Preprint. Discussion started: 29 September 2026

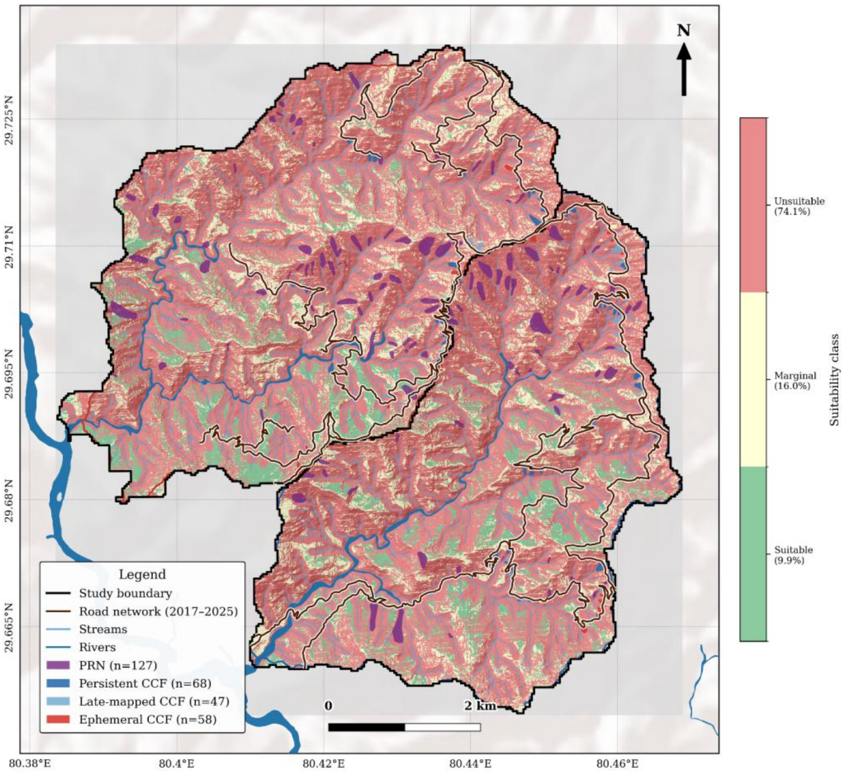

Figure 15: Suitability map with the 173 CCF.

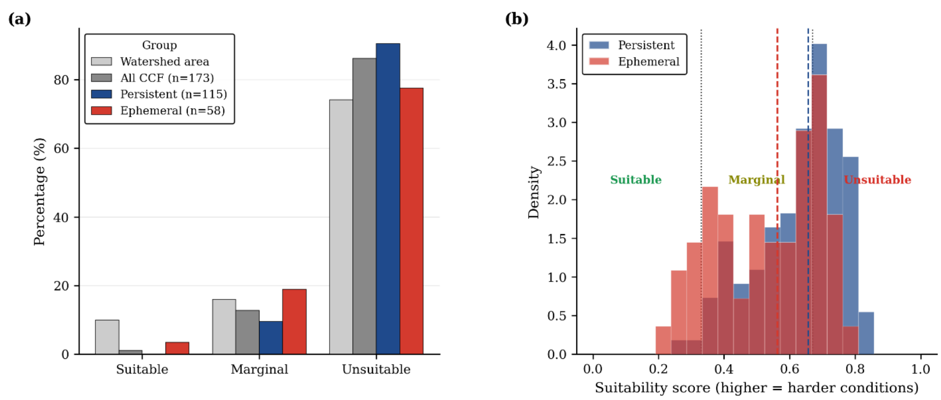

Figure 16: Persistence classes across suitability zones.

Table 6: Suitability zones: area and distribution of all, persistent, ephemeral failures.

https://doi.org/10.5194/egusphere-2026-4364
Preprint. Discussion started: 29 September 2026

Zone	Area (ha)	% watershed	All CCF n (%)	Persistent n (%)	Ephemeral n (%)
Suitable	457.3	9.9	2 (1.2)	0 (0.0)	2 (3.4)
Marginal	737.6	16.0	22 (12.7)	11 (9.6)	11 (19.0)
Unsuitable	3,425.9	74.1	149 (86.1)	104 (90.4)	45 (77.6)

5 Discussion

5.1 Road construction as the primary trigger

"Construction-coincident" is an observational label: a failure that appeared on a construction date, within tens of metres of the active front. The stronger claim that construction triggered it depends on ruling out rain. Rainfall was absent on 63.6 % of failures by gauge and 78.6 % by CHIRPS, and where the two sources disagree the satellite more often places the failure pixel dry than the reverse. Antecedent totals were low, and event-day rainfall was zero where Dahal and Hasegawa (2008) put the daily threshold for rainfall-triggered failure in the Nepal Himalaya near 144 mm. No rainfall–failure correlation held at any timescale under either source. Direct causation cannot be shown by remote sensing, but rainfall, the main alternative, is excluded for most of the failures.

Emmer et al. (2022) came closest in prior work, matching daily imagery and rainfall to road-corridor failures in Peru, but could not separate genuine failures from dumped spoil, which looks the same. This study does not resolve that either; it treats spoil-loaded failures as part of the construction-disturbance population. What it adds is the rainfall exclusion under two independent sources. The three heavy-rain failures fit the reduced factor of safety that cuts impose (Pradhan et al., 2022): a cut slope needs less rain to fail than an intact one.

5.2 Proximity to the construction front

Failures fell within 50 m of the same-day front in 87.3 % of cases, against 28.9 % for the older road. This is tighter than the disturbance envelopes reported for completed roads, which extend to about 100 m in Sindhupalchok (McAdoo et al., 2018) and 150 m in

https://doi.org/10.5194/egusphere-2026-4364
Preprint. Discussion started: 29 September 2026

southern Ecuador (Brenning et al., 2015), and it places the failures at the active face rather than across the wider envelope of a finished road. Daily failure count also rose with daily road length, linking more failures to larger same-day advances.

5.3 A distinct failure population

CCF were smaller, less elongate, and on gentler slopes than the pre-road failures, marking them as freshly disturbed cut-face and spoil material rather than the larger natural detachments. This matches Robson et al. (2022), who report that most mountain-road failures in Nepal are shallow cut-slope instabilities. CCF also sat on wetter ground than the natural failures, concentrating on convergent terrain.

5.4 Misattribution in quarterly inventories

Of the 115 failures that entered the inventory, 60.0 % occurred on dry days, and three of the five monsoon-quarter Persistent failures failed on dry days. An inventory would record these as monsoon failures. The error is structural: the trigger acts at daily resolution while the inventory records at quarterly resolution. A monsoon-rainfall signal drawn from inventory data, as in Muñoz-Torrero Manchado et al. (2021), may therefore be inflated by construction failures that happen to fall in the rainy season. A second of every three failures was ephemeral and never reached the inventory at all, so the true extent of construction disturbance exceeds any inventory-based count.

5.5 Controls on persistence

Area and south-facing aspect were the strongest controls, agreeing across the LASSO, Random Forest, and SHAP. Larger failures persist more often, which fits the size association Chen et al. (2024) report for persistent Himalayan failures. Persistent failures sat on south-facing slopes; this aligns with the aspect–revegetation link Chen et al. (2024) note, though the data establish the association, not its cause. Proximity to thrust faults fits the higher phyllite content and deformation near thrust zones (DeCelles et al., 2001). The rainfall predictors carried little weight, consistent with the trigger result: rainfall is not what controls whether a failure persists.

5.6 Suitability and policy

https://doi.org/10.5194/egusphere-2026-4364
Preprint. Discussion started: 29 September 2026

Persistent failures fell in Unsuitable terrain in 90.4 % of cases, and the hold-out held at 90.0 % on an unseen watershed, so the sites most prone to persistent failure can be identified before a road is cut. The practical value lies in the timing: the four mapped variables, namely (i) aspect, (ii) slope, (iii) distance to thrust, and (iv) elevation, are all knowable from a digital elevation model and geological map before any excavation, so the assessment can guide a route or a spoil-disposal plan at the design stage rather than after failures appear. This matters because pre-construction assessment is largely absent on Nepal's rural roads: the Rural Road Standards carry no slope-excavation guidelines and leave spoil disposal unregulated (Paudyal et al., 2023), and existing guidance is applied unevenly (Robson et al., 2025). In the study watersheds, only a quarter of the terrain (the Suitable and Marginal classes) would be available for spoil at lower persistent-failure risk, which is itself a planning constraint worth knowing in advance. The positive coefficient on daily road length points to a second, simpler lever that needs no map: slowing the daily rate of advance may reduce both the number of failures and the share that persist, since both rose with how much road was cut in a day.

5.7 Limitations

The study covers two adjacent watersheds; transfer held between them, but a test in a different lithology and climate is needed for full generalisation. The modest AUC reflects the binary framing of a continuous process, and some ephemeral failures may reflect detection limits rather than true revegetation, though the narrow threshold range bounds this. One monsoon failure (10 July 2019) fell on fully clouded imagery and could not be confirmed; its date carries the widest uncertainty in the dataset. Two predictors were limited by coverage: soil data, excluded, and the spectral index, available for most but not all failures.

6 Conclusions

This study provides daily-resolution evidence that road construction, not rainfall, triggered most slope failures along a new mountain road in Far-West Nepal. Of 173 construction-coincident failures over nine years, 63.6 % occurred with no rainfall by gauge and 78.6 % by satellite, none correlated with rainfall at any timescale, and the failures tracked the active

https://doi.org/10.5194/egusphere-2026-4364
Preprint. Discussion started: 29 September 2026

works rather than the existing road: 87.3 % fell within 50 m of the same-day construction front, against 28.9 % of the older road. They also formed a population distinct from the pre-road natural failures, smaller and less elongate.

The contribution is not daily imagery alone, which Emmer et al. (2022) also used, but its combination with two independent rainfall sources, a multi-year persistence classification, and a validated pre-construction suitability map. One in three failures never entered the quarterly inventory, and 60 % of those that did had failed on dry days, so inventory-based attribution misassigns construction failures to the monsoon. Whether a failure persists proved predictable from the site: south-facing aspect and failure size were the dominant and most stable controls, and a map built from four variables knowable before construction placed about 90 % of persistent failures in terrain flagged unsuitable beforehand, holding on an unseen watershed. Directing spoil away from such terrain, and slowing the daily rate of construction, are two measures available before a road is built.

Because these failures are caused by construction rather than rainfall, they are in principle preventable: unlike rain-driven landslides, they depend on how the slope is cut and where the spoil is placed, both under human control. The pre-construction map relies on four variables, aspect, slope, distance to thrust, and elevation, all readable from a digital elevation model and a geological map, so terrain can be analysed at the design stage without field survey. The same conditions occur wherever rural roads are pushed into steep terrain without slope assessment or spoil control, as across South and Southeast Asia, Latin America, and sub-Saharan Africa. The specific weights would need recalibrating elsewhere, but the approach transfers to any mountain region facing the same road expansion. For the communities living below these roads, much of this damage is not an unavoidable hazard but a consequence of how the roads are built, and one that better practice could largely prevent.

7 Code and data availability

All analysis was performed in PyGILE-Plus v1.1.0 (Awasthi et al., 2026) archived on Zenodo at https://doi.org/10.5281/zenodo.18512474.

https://doi.org/10.5194/egusphere-2026-4364
Preprint. Discussion started: 29 September 2026

The derived datasets supporting this study namely (a) daily road-construction lines, (b) daily and pre-road landslide-failure polygons, (c) the quarterly landslide inventory, and (d) the attribute table of construction-coincident failures are archived on Zenodo. It can be accessed at https://doi.org/10.5281/zenodo.21456421 and are under embargo until 31 March 2027, as they underpin a forthcoming companion study; access before that date may be arranged with the corresponding author.

PlanetScope imagery was accessed under Planet's Education and Research Program and cannot be redistributed; it is available from Planet (https://www.planet.com). CHIRPS rainfall data are publicly available (Funk et al., 2015). Raw daily rain-gauge records are held by the Department of Hydrology and Meteorology, Government of Nepal, and are subject to its data-sharing policy; only the derived rainfall classifications are included in the archived dataset.

8 Author contributions

BA conceptualised the study, performed the analysis, and wrote the manuscript. SN, NKT, and KCC supervised the work and reviewed and edited the manuscript. All authors have read and agreed to the submitted version.

9 Competing interests

The authors declare that they have no conflict of interest.

10 Acknowledgements

We would like to acknowledge Planet's Education and Research Program for providing access to PlanetScope imagery. During the preparation of this work, Claude Sonnet 4.5 (Anthropic) was utilized for grammar and language refinement and for assistance with coding. The study's concept, design, analysis, and interpretations are the authors' own, and the authors take full responsibility for the content of this work.

11 Financial support

This research was carried out in partial fulfilment of the requirements for a PhD at the Asian Institute of Technology, supported by a Government of Japan scholarship administered by AIT. The scholarship provided no dedicated funding for publication.

https://doi.org/10.5194/egusphere-2026-4364
Preprint. Discussion started: 29 September 2026

12 References

Awasthi, B., Ninsawat, S., Raghavan, V., and Nemoto, T.: Python GeoInformatics Lab Environment-Plus, https://github.com/Geoinformatics-Lab/PyGILE-Plus, 2026.

Beyer, R. A., Alexandrov, O., and McMichael, S.: The Ames Stereo Pipeline: NASA's Open Source Software for Deriving and Processing Terrain Data, Earth and Space Science, 5, 537–548, https://doi.org/10.1029/2018EA000409, 2018.

Brenning, A., Schwinn, M., Ruiz-Páez, A. P., and Muenchow, J.: Landslide susceptibility near highways is increased by 1 order of magnitude in the Andes of southern Ecuador, Loja province, Natural Hazards and Earth System Sciences, 15, 45–57, https://doi.org/10.5194/nhess-15-45-2015, 2015.

Chen, T.-H. K., Kincey, M. E., Rosser, N. J., and Seto, K. C.: Identifying recurrent and persistent landslides using satellite imagery and deep learning: A 30-year analysis of the Himalaya, Science of The Total Environment, 922, 171161, https://doi.org/10.1016/j.scitotenv.2024.171161, 2024.

Dahal, R. K. and Hasegawa, S.: Representative rainfall thresholds for landslides in the Nepal Himalaya, Geomorphology, 100, 429–443, https://doi.org/10.1016/j.geomorph.2008.01.014, 2008.

DeCelles, P. G., Robinson, D. M., Quade, J., Ojha, T. P., Garzione, C. N., Copeland, P., and Upreti, B. N.: Stratigraphy, structure, and tectonic evolution of the Himalayan fold-thrust belt in western Nepal, Tectonics, 20, 487–509, https://doi.org/10.1029/2000TC001226, 2001.

Emmer, A., Hölbling, D., Abad, L., Štěpánek, P., Zahradníček, P., and Emmerová, I.: Landslides associated with recent road constructions in the Río Lucma catchment, eastern Cordillera Blanca, Peru, An. Acad. Bras. Cienc., 94, https://doi.org/10.1590/0001-3765202220211352, 2022.

European Space Agency: Copernicus DEM, https://doi.org/10.5270/ESA-c5d3d65, 2022.

Fookes, P. G., Sweeney, M., Manby, C. N. D., and Martin, R. P.: Geological and geotechnical engineering aspects of low-cost roads in mountainous terrain, Eng. Geol., 21, 1–152, https://doi.org/10.1016/0013-7952(85)90002-X, 1985.

https://doi.org/10.5194/egusphere-2026-4364
Preprint. Discussion started: 29 September 2026

Froude, M. J. and Petley, D. N.: Global fatal landslide occurrence from 2004 to 2016, Natural Hazards and Earth System Sciences, 18, 2161–2181, 2018.

Funk, C., Peterson, P., Landsfeld, M., Pedreros, D., Verdin, J., Shukla, S., Husak, G., Rowland, J., Harrison, L., Hoell, A., and Michaelsen, J.: The climate hazards infrared precipitation with stations—a new environmental record for monitoring extremes, Sci. Data, 2, 150066, https://doi.org/10.1038/sdata.2015.66, 2015.

Guzzetti, F., Peruccacci, S., Rossi, M., and Stark, C. P.: The rainfall intensity–duration control of shallow landslides and debris flows: an update, Landslides, 5, 3–17, 2008.

Harvey, E. L., Kincey, M. E., Rosser, N. J., Gadtaula, A., Collins, E., Densmore, A. L., Dunant, A., Oven, K. J., Arrell, K., Basyal, G. K., Dhital, M. R., Robinson, T. R., Van Wyk de Vries, M., Paudyal, S., Pujara, D. S., and Shrestha, R.: Review of landslide inventories for Nepal between 2010 and 2021 reveals data gaps in global landslide hotspot, https://doi.org/10.1007/s11069-024-07013-1, 1 March 2025.

Hearn, G. J. and Shakya, N. M.: Engineering challenges for sustainable road access in the himalayas, Quarterly Journal of Engineering Geology and Hydrogeology, 50, 69–80, https://doi.org/10.1144/qjegh2016-109, 2017.

Laurance, W. F., Clements, G. R., Sloan, S., O'Connell, C. S., Mueller, N. D., Goosem, M., Venter, O., Edwards, D. P., Phalan, B., Balmford, A., Van Der Ree, R., and Arrea, I. B.: A global strategy for road building, Nature, 513, 229–232, https://doi.org/10.1038/nature13717, 2014.

Marc, O. and Hovius, N.: Amalgamation in landslide maps: effects and automatic detection, Natural Hazards and Earth System Sciences, 15, 723–733, https://doi.org/10.5194/nhess-15-723-2015, 2015.

McAdoo, B. G., Quak, M., Gnyawali, K. R., Adhikari, B. R., Devkota, S., Lal Rajbhandari, P., and Sudmeier-Rieux, K.: Roads and landslides in Nepal: How development affects environmental risk, Natural Hazards and Earth System Sciences, 18, 3203–3210, https://doi.org/10.5194/nhess-18-3203-2018, 2018.

Mey, J., Guntu, R. K., Plakias, A., Silva De Almeida, I., and Schwanghart, W.: More than one landslide per road kilometer - surveying and modeling mass movements along the

https://doi.org/10.5194/egusphere-2026-4364
Preprint. Discussion started: 29 September 2026

Rishikesh-Joshimath (NH-7) highway, Uttarakhand, India, Natural Hazards and Earth System Sciences, 24, 3207–3223, https://doi.org/10.5194/nhess-24-3207-2024, 2024.

Muñoz-Torrero Manchado, A., Allen, S., Ballesteros-Cánovas, J. A., Dhakal, A., Dhital, M. R., and Stoffel, M.: Three decades of landslide activity in western Nepal: new insights into trends and climate drivers, Landslides, 18, 2001–2015, https://doi.org/10.1007/s10346-021-01632-6, 2021.

Neuenschwander, A. and Pitts, K.: The ATL08 land and vegetation product for the ICESat-2 Mission, Remote Sens. Environ., 221, 247–259, https://doi.org/10.1016/j.rse.2018.11.005, 2019.

Nuth, C. and Kääb, A.: Co-registration and bias corrections of satellite elevation data sets for quantifying glacier thickness change, Cryosphere, 5, 271–290, https://doi.org/10.5194/tc-5-271-2011, 2011.

Paudyal, P., Dahal, P., Bhandari, P., and Dahal, B. K.: Sustainable rural infrastructure: guidelines for roadside slope excavation, Geoenvironmental Disasters, 10, https://doi.org/10.1186/s40677-023-00240-x, 2023.

Peduzzi, P., Concato, J., Kemper, E., Holford, T. R., and Feinstein, A. R.: A simulation study of the number of events per variable in logistic regression analysis, J. Clin. Epidemiol., 49, 1373–1379, https://doi.org/10.1016/S0895-4356(96)00236-3, 1996.

Planet Application Program Interface: In Space for Life on Earth: https://api.planet.com, last access: 4 April 2026.

Pradhan, S., Toll, D., Rosser, N., and Brain, M.: An Investigation of the Combined Effect of Rainfall and Road Cut on Landsliding, Social Science Research Network, https://doi.org/10.2139/ssrn.4010371, 2022.

Robinson, D. and DeCelles, P.: Finding the lesser himalayan duplex in the himalayan thrust belt of far western Nepal amidst forests, villages, farming and leeches, Journal of the Virtual Explorer, 47, https://doi.org/10.3809/jvirtex.2014.00341, 2014.

Robson, Dahal, B. K., and Toll, D. G.: A participatory approach to determine the use of road cut slope design guidelines in Nepal to lessen landslides, Natural Hazards and Earth System Sciences, 25, 949–973, https://doi.org/10.5194/nhess-25-949-2025, 2025.

https://doi.org/10.5194/egusphere-2026-4364
Preprint. Discussion started: 29 September 2026

Robson, E., Agosti, A., Utili, S., and Milledge, D.: A methodology for road cutting design guidelines based on field observations, Eng. Geol., 307, https://doi.org/10.1016/j.enggeo.2022.106771, 2022.

Sidle, R. C., Furuichi, T., and Kono, Y.: Unprecedented rates of landslide and surface erosion along a newly constructed road in Yunnan, China, Natural Hazards, 57, 313–326, https://doi.org/10.1007/s11069-010-9614-6, 2011.

van Smeden, M., Moons, K. G., de Groot, J. A., Collins, G. S., Altman, D. G., Eijkemans, M. J., and Reitsma, J. B.: Sample size for binary logistic prediction models: Beyond events per variable criteria, Stat. Methods Med. Res., 28, 2455–2474, https://doi.org/10.1177/0962280218784726, 2019.

Stanley, T. A., Kirschbaum, D. B., Benz, G., Emberson, R. A., Amatya, P. M., Medwedeff, W., and Clark, M. K.: Data-Driven Landslide Nowcasting at the Global Scale, Front. Earth Sci. (Lausanne)., 9, https://doi.org/10.3389/feart.2021.640043, 2021.

Sudmeier-Rieux, K., McAdoo, B. G., Devkota, S., Chandra Lal Rajbhandari, P., Howell, J., and Sharma, S.: Invited perspectives: Mountain roads in Nepal at a new crossroads, Natural Hazards and Earth System Sciences, 19, 655–660, https://doi.org/10.5194/nhess-19-655-2019, 2019.

Tadono, T., Ishida, H., Oda, F., Naito, S., Minakawa, K., and Iwamoto, H.: Precise Global DEM Generation by ALOS PRISM, ISPRS Annals of the Photogrammetry, Remote Sensing and Spatial Information Sciences, II–4, 71–76, https://doi.org/10.5194/isprsannals-II-4-71-2014, 2014.

Zhao, Y., Huang, Y., Liu, H., Wei, Y., Lin, Q., and Lu, Y.: Use of the Normalized Difference Road Landside Index (NDRLI)-based method for the quick delineation of road-induced landslides, Sci. Rep., 8, https://doi.org/10.1038/s41598-018-36202-9, 2018.